

A neutral strongly coupled laser-produced plasma by strong-field ionization in a gas jet

S. D. Bergeson, M. Lyon, J. B. Peatross, N. Harrison, D. Crunkleton, J. Wilson, S. Rupper, A. Diaw, and M. S. Murillo

Citation: [AIP Conference Proceedings](#) **1668**, 040001 (2015); doi: 10.1063/1.4923114

View online: <http://dx.doi.org/10.1063/1.4923114>

View Table of Contents: <http://scitation.aip.org/content/aip/proceeding/aipcp/1668?ver=pdfcov>

Published by the [AIP Publishing](#)

Articles you may be interested in

[Influence of magnetic field on laser-produced barium plasmas: Spectral and dynamic behaviour of neutral and ionic species](#)

J. Appl. Phys. **116**, 153301 (2014); 10.1063/1.4898132

[Characteristics of laser-produced plasmas in a gas filled chamber and in a gas jet by using a long pulse laser](#)

J. Appl. Phys. **94**, 5497 (2003); 10.1063/1.1614427

[Polarization spectroscopic imaging of charge separation in neutral gas-confined laser-produced plasmas](#)

Rev. Sci. Instrum. **74**, 2123 (2003); 10.1063/1.1537446

[CO₂-laser-produced plasma-initiated neutral-gas recombination lasers](#)

J. Appl. Phys. **50**, 7921 (1979); 10.1063/1.325967

[Collisional coupling in counterstreaming laser-produced plasmas](#)

Phys. Fluids **17**, 1560 (1974); 10.1063/1.1694934

A Neutral Strongly Coupled Laser-Produced Plasma by Strong-Field Ionization in a Gas Jet

S. D. Bergeson*, M. Lyon*, J. B. Peatross*, N. Harrison*, D. Crunkleton*, J. Wilson*, S. Rupper*, A. Diaw[†] and M. S. Murillo[†]

**Department of Physics and Astronomy, Brigham Young University, Provo, UT 84602, USA*

[†]*New Mexico Consortium, Los Alamos, New Mexico 87544, USA*

Abstract. We report measurements of a neutral strongly coupled plasma generated by focusing a femtosecond-duration laser pulse into a room-temperature gas jet. The ion temperature in this plasma is determined by the plasma density through the disorder-induced heating effect. We present measurements of the mass, radius, and energy dependence of the time-varying ion density as the plasma expands. Molecular dynamics model indicate that higher values of the strong coupling parameter could be achieved if the plasma is ionized again by a second laser pulse that follows the first one. However, the final value of the coupling parameter appears to be only weakly dependent on the final ionization state.

Keywords: plasma, ultracold, disorder induced heating, strongly coupled

PACS: 52.27.Gr, 52.25.-b

INTRODUCTION

Strong coupling is a condition that exists in many areas of physics, across a wide range of temperature and density. It appears when the nearest-neighbor interaction energy exceeds the mean kinetic energy in a system. Electrons in a metal, for example, are strongly coupled. Other examples include the quark-gluon plasma [1], the interior of Jovian planets and the crusts of white dwarf stars [2], strong atomic interactions in the BEC-BCS cross-over [3], the Mott-insulator transition [4], warm dense matter [5], dusty and non-neutral plasmas [6, 7], and certain classes of laser-matter interactions.

For Coulomb-coupled systems, the degree of coupling can be estimated using the strong-coupling parameter,

$$\Gamma = \frac{Z^2 e^2}{4\pi\epsilon_0 a_{ws} k_B T}, \quad (1)$$

where Z is the ion charge state, e is the fundamental charge, ϵ_0 is the permittivity of free space, $a_{ws} = (3/4\pi n)$ is the Wigner-Seitz radius (or mean distance between particles), n is the particle density, k_B is Boltzmann's constant, and T is the ion temperature. Generally speaking, the condition $\Gamma = 1$ corresponds to a non-ideal plasma in which the number of particles per Debye sphere is small and the traditional assumptions regarding shielding, kinetic transport, etc., are no longer valid. This is an interesting and technologically important regime, one approximated in certain classes of fusion-class plasmas.

The $\Gamma > 1$ regime is interesting in large measure because of the kinds of collisions that occur. In kinetic theories, collisions are represented by the traditional two-body collision formulas modified with a Coulomb logarithm. This modification occurs because the Coulomb collision cross section diverges due to the long-range nature of charged-particle collisions. This divergence is avoided by choosing both minimum and maximum impact parameters beyond which collisions are expected to be negligible (at long-distances) or rare (at short distances). However, when $\Gamma = 1$, these cut-offs become problematic. The long-range cut-off is the Debye length. The short-range cut-off is the classic distance of closest approach. When $\Gamma = 1$, these two distances become comparable to each other, both of them approaching the Wigner-Seitz radius. In this limit, the ions are constantly colliding and simple applications of kinetic equations produces nonsensical results.

It is possible to extend kinetic theories using molecular-dynamics simulations or effective potential theories [8]. Recent computational and theoretical work has shown good agreement, suggesting that this combination of approaches can help to extend our understanding of strongly-coupled Coulomb systems.

TABLE 1. The ion and electron plasma frequencies (ω_p^i and ω_p^e) and correlation temperature for a few different densities in neon. The plasma frequency scales as $n^{1/2}$. The correlation temperature scales as $n^{1/3}$.

Density (cm^{-3})	ω_p^i	ω_p^e	T_c (K)
10^9	1×10^7	2×10^9	1
10^{12}	3×10^8	6×10^{10}	10
10^{15}	1×10^{10}	2×10^{12}	100
10^{18}	3×10^{11}	6×10^{13}	1000
10^{21}	1×10^{13}	2×10^{15}	10,000

One of the major priorities in the field of strongly coupled neutral Coulomb systems is to extend the accessible range of Γ values. Most work at the present is limited to the range of $\Gamma \sim 1 - 5$ [9, 10], although higher values may be possible using Rydberg or molecular systems [11, 12]. When the value of Γ is high enough, new phenomena appear in plasmas. These include the emergence of shear waves not normally allowed in plasma systems [13, 14, 15], solidification [16], cooperative behavior [17], and anomalous transport [18]. Collision properties change, and correlations lead to an increased probability of collisions with small impact parameters [19, 20, 21]. When the density and temperature are high enough, these collisions are predicted to lead to exponential enhancement in thermonuclear fusion rates [22, 23, 24, 25].

In this paper we present measurements of the time-dependent density of a plasma generated by focusing a femtosecond (fs)-duration laser pulse into a room-temperature gas jet. We illustrate the density's dependence the ion mass, initial electron energy, and initial distribution radius. The ion temperature in this plasma is determined by the plasma density through the disorder-induced heating effect [9, 26, 27, 28, 29]. We present measurements of the mass, radius, and energy dependence of the time-varying ion density. We present the results from an molecular dynamics model indicating that higher Γ can be achieved if the plasma is ionized by a second laser pulse. However, the new Γ appears to be only weakly dependent on the final ionization state.

ULTRACOLD NEUTRAL PLASMAS AT ROOM TEMPERATURE

Our laser-produced plasmas are similar in some respects to ultracold neutral plasmas (UNPs). One of the defining features of most UNPs is that the ion temperature is determined exclusively by the density [28]. This happens because of disorder-induced heating. Ultracold plasmas are typically formed by photo-ionizing laser-cooled atoms, or by exciting atoms and molecules in a supersonic expansion [28, 30, 31, 32]. In the case of laser-cooled atoms, the neutral atom temperature is typically a few mK. When the atoms are ionized, the atom-atom interaction suddenly increases. Although the ions have essentially zero kinetic energy, they have a comparatively large electrical potential energy. The ions move to minimize this potential energy, converting some of it into thermal energy. This process is called disorder-induced heating (DIH). In the absence of correlation effects, the characteristic temperature after the ion distribution initially relaxes is given approximately by equating the average nearest-neighbor potential energy to temperature [28],

$$k_B T_c = \frac{2}{3} \frac{e^2}{4\pi\epsilon_0 a_{ws}}. \quad (2)$$

Table 1 shows how this characteristic temperature depends on density. For laser-cooled atom densities, the temperature after DIH is in the 0.5 to 10 K range.

We recently published a study of the density evolution in a strongly coupled neutral plasma generated by focusing a fs-duration laser pulse into a room-temperature gas jet [33]. We showed that the ultracold neutral plasma expansion model described this higher-temperature strongly coupled system well, and that it could be used to extract an electron temperature.

In this paper, we discuss a few more details of this system. The plasmas are created by strong-field ionization of noble gas atoms in the gas jet. The initial density of our plasma is $n > 10^{18} \text{ cm}^{-3}$. Using Eq. 2, the post-DIH ion temperature is expected to be greater than 1000 K. For this reason, our plasmas enter the same parameter space as the ultracold neutral plasmas, even though the temperatures and densities are far from those in UNPs.

TABLE 2. Laser intensities, I_α (W/cm^{-2}), required to reach different ionization stages in He, Ne, and Ar.

Z	He	Ne	Ar
1	1.3×10^{15}	8.7×10^{14}	2.5×10^{14}
2	8.7×10^{15}	2.8×10^{15}	5.8×10^{14}
3	...	7.2×10^{15}	1.2×10^{15}
4	...	2.2×10^{16}	3.2×10^{15}
5	...	4.0×10^{16}	5.1×10^{15}

Another important similarity between our plasmas and “traditional” UNPs is that the ionization step is on the order of the shortest time scales in the plasma. The electron and ion plasma frequencies depend on density and are given in Table 1. For a density of $n = 10^{18} \text{ cm}^{-3}$, they are $\omega_p^i = 3 \times 10^{11} \text{ s}^{-1}$ and $\omega_p^e = 6 \times 10^{13} \text{ s}^{-1}$ for neon. Our laser pulse duration is $\tau_L = 70 \text{ fs}$, making τ_L^{-1} on the same order as the electron plasma frequency and much shorter than the ion plasma frequencies. This is also true for many UNPs created by ns-duration laser pulses. As we will show later in this paper, the electron energy in our plasmas is in the 10 eV range and ponderomotive heating of the electrons and ions is negligible. There is no direct heating of the ions by the laser pulse itself.

In ultracold neutral plasmas, the characteristic time scales for thermalization and heating fall into a certain hierarchy. For example, consider a singly-ionized neon plasma at a density of 10^{18} cm^{-3} , generated by a laser pulse focused to $10 \mu\text{m}$. The electrons thermalize quickly, on the time scale of the electron plasma period, $(\omega_p^e)^{-1} = 14 \text{ fs}$. This is followed by ion thermalization after roughly one ion plasma period, $(\omega_p^i)^{-1} = 3 \text{ ps}$. The time scale for plasma expansion is roughly $r_0/v_e = 10^{-5} \text{ m}/7000 \text{ m/s} = 1.4 \text{ ns}$, where the expansion velocity is $v_e = (k_B T_e/m_i)^{1/2}$, the electron temperature is T_e , the ion mass is m_i , and we have assumed a $k_B T_e = 10 \text{ eV}$.

Strong-field ionization

Our plasmas are created when we focus a short laser pulse into a gas jet. The laser intensity is high enough that the electric field in the laser focus is stronger than the Coulomb field experienced by the bound-state electrons. The Coulomb field becomes a perturbation to the laser field, and the electrons act as a free electron gas. The laser intensities at which ionization occurs follow the formula

$$I_\alpha = \left(4.00 \times 10^9 \frac{\text{W}}{\text{cm}^2 \cdot \text{eV}^4} \right) \frac{\Phi^4}{Z^2} \quad (3)$$

where α will be used to designate the gas species and ionization state and Φ is the binding energy in eV. The intensity I_α is given for a range of gases and ionization states in Table 2.

In strong-field ionization, the laser field overwhelms the Coulomb field to such an extent that the bound state appears in the continuum [34]. We will write down the potential for the electron in the presence of the ion and the laser field,

$$U(t) = -\frac{Ze^2}{4\pi\epsilon_0|x|} - eE_0x \cos(\omega_L t), \quad (4)$$

where ω_L is the laser frequency and E_0 is the laser electric field. When $t = 0$, the potential is shown in Fig. 1.

We can solve for the value of x where the total potential in Eq. 4 is (locally) maximized. By setting this equal to the bound state potential for the electron, we can solve for the electric field necessary to ionize the atom,

$$E_0 = \frac{\pi\epsilon_0}{Ze^3} \Phi^2. \quad (5)$$

If this equation is converted to atomic units, we reproduce the equation for (DC) strong-field ionization in Rydberg atoms, $E_0 = \frac{1}{16s^4}$, where s is the Rydberg atom’s principle quantum number. It is important to remember, however, that in all cases strong-field ionization occurs when the electric field is more or less static on the time scale of the electron

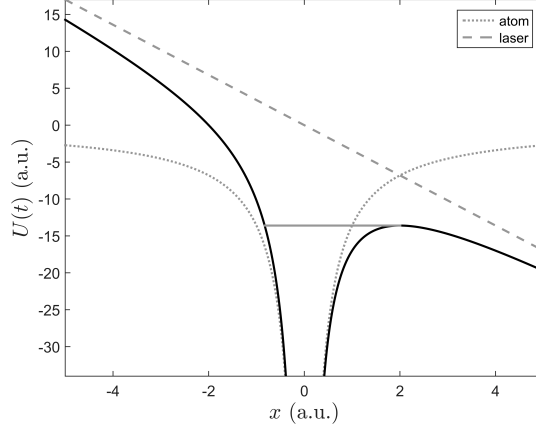


FIGURE 1. The total potential for the electron, $U(t)$, when $\omega_L t = \pi$, plotted as a solid black line. Also plotted are the potential from the parent ion and the laser. The energy of a bound state is represented by the horizontal solid gray line. When the local maximum of the combined potential equals the electron binding potential in the unperturbed atom ($x = 2$ in this plot), ionization occurs.

motion. The minimum laser intensity for ionization of ground-state atoms is

$$I = \frac{1}{2} c \epsilon_0 E_0^2 = \frac{\pi^2 c \epsilon_0^3 \Phi^4}{2e^6 Z^2}. \quad (6)$$

Plugging in numerical values for the constants gives Eq. 3.

The electron energy

For an isolated charged particle, and when the laser intensity is results in non-relativistic electron motion, the interaction with an oscillating electric field is conservative. Although an electron can experience a ponderomotive energy of hundreds of eV in the focus of the high intensity laser, an electron initially at rest will be brought back to rest when the laser pulse is over.

The electron in the presence of the laser field experiences an acceleration,

$$\ddot{x} = \frac{eE(t)}{m_e} \cos(\omega_L t + \phi), \quad (7)$$

where $E(t)$ is the time-dependent field (envelope function) and m_e is the electron mass. The speed of the electron is

$$\dot{x} = \frac{eE}{\omega_L m_e} [\sin(\omega_L t + \phi) - \sin(\theta)]. \quad (8)$$

The angle θ corresponds to the phase in the laser pulse at which the electron breaks away from the parent ion. In our model of strong-field ionization, the electrons are liberated at a turning point in the Coulomb potential, and therefore can be considered as starting at rest.

Integrating the equations of motion for the electron in the field shows that if the electron breaks away at $\theta = 0$, it will come to rest at the end of the laser pulse. In actuality, the electron breaks away for a small range of angles relative to $\theta = 0$. When the laser pulse is over, the electron retains the “extra” drift velocity in Eq. 8,

$$v_{\text{drift}} = \frac{eE(t_0)}{\omega_L m_e} \sin \theta, \quad (9)$$

where $E(t_0)$ is the value of the field at the moment the electron breaks away. The kinetic energy associated with this drift velocity is

$$K_{\text{drift}} = 2U_p \sin^2 \theta, \quad (10)$$

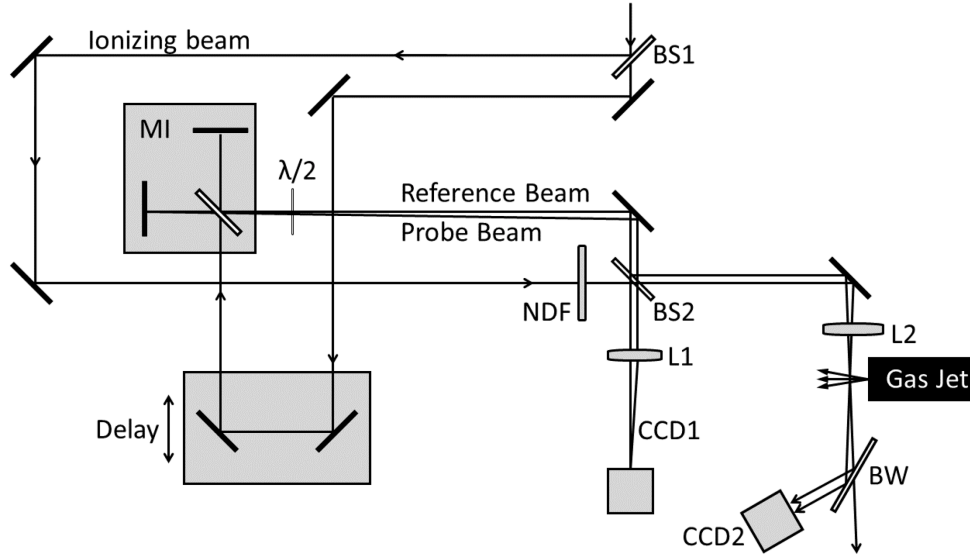


FIGURE 2. Schematic diagram of the experiment. A strong laser pulse enters the apparatus from the top of this diagram. Most of the pulse is split off using a 95%/5% beamsplitter. This strong pulse is focused into the gas jet to form the plasma. The weaker 5% pulse is sent through a delay line and then a slightly misaligned Michelson interferometer, generating a probe and reference beam. BS1/BS2 = beam splitter, MI = Michelson interferometer, $\lambda/2$ = half-wave-plate, NSF = neutral density filter, L1/L2 lenses, BW = Brewster window.

where $U_p = (e^2 E^2 / 4m_e \omega_L^2)$ is the ponderomotive energy of the electron in the laser field.

In determining the final energy, this kinetic energy is averaged over the likely range of release angles, θ ,

$$\langle K_{\text{drift}} \rangle = 2U_p \langle \sin^2 \theta \rangle = \frac{U_p}{2\theta_{\text{max}}} \int_{-\theta_{\text{max}}}^{\theta_{\text{max}}} \sin^2 \theta d\theta = U_p \left(1 - \frac{\sin 2\theta_{\text{max}}}{2\theta_{\text{max}}} \right) \approx \frac{2}{3} U_p \theta_{\text{max}}^2. \quad (11)$$

The classical “over-the-barrier” model described in Eqs. 3 through 6 presents an overly simplistic picture of the ionization process. Ionization is a tunneling process and portions of the electron wavepacket are released on repeated cycles of the laser field. Numerical simulations suggest that ionization requires several laser cycles to complete, with most of the electron wavepacket release occurring when the field is strongest. Estimates of θ_{max} suggest that the electron energy should be on the order of $0.1U_p$, where U_p corresponds to the ponderomotive energy of the electron in the field at which ionization occurs. This estimate is roughly consistent with earlier electron energy measurements [35].

The laser system

A schematic diagram showing the laser path is shown in Fig. 2 [33]. The plasma is generated by focusing Ti:sapphire laser (pulse energy up to 8 mJ, pulse duration 70 fs) into a pulsed gas jet. Depending on the focusing lens used, the Gaussian beam waist at the laser focus is 10 to 25 μm . The atom density in the jet ranges up to $n \sim 10^{19} \text{cm}^{-3}$. The jet is formed using a solenoid valve with a 300 μm diameter and 2 mm length tube serving as the nozzle. While this lengthens the duration of the gas pulse, it defines the geometry of the jet and therefore the spatial length of the plasma. The gas fans out from the jet and has a width of ~ 1 mm where the ionizing laser passes through it. The pressure behind the solenoid is 900 Torr at 20° C.

The laser pulse is split using a 95%/5% beamsplitter. Most of the pulse energy is focused into the gas jet to generate the plasma. The weaker portion of the beam is sent through an optical delay line and a Michelson interferometer. The interferometer is slightly misaligned so that it generates two output laser beams, called a “probe” and “reference” beam. The beam separation is typically less than 0.1° . One of the mirrors in the Michelson interferometer is mounted onto a translation stage, and the interferometer is set to zero path length difference. These two beams are expanded by a factor of two in diameter using a Galilean telescope, so that they will focus to a smaller diameter than the ionizing

beam. The probe and reference beams are combined with the strong laser pulse on a beamsplitter, and the probe beam aligned to exactly coincide with the ionizing beam. All three pulses are focused into the plasma. The strong pulse generates the plasma. The probe beam passes through the plasma. The reference beam passes through the un-ionized gas, approximately 1 mm farther from the jet nozzle than the plasma.

Roughly half of the light from BS2, the beamsplitter used to recombine the laser beams, passes through the gas jet. The other half is used for alignment. These laser beams are strongly attenuated using a neutral density filter (not shown in Fig. 2) and are focused onto a CCD camera (CCD1 in Fig. 2). Small alignment adjustments are made using BS2 to overlap the probe and ionizing laser pulses on CCD1. The symmetry of the optical path ensures that these laser beams will also be overlapped at the focus of L2 in the gas jet.

Because the probe/reference and ionizing beams have orthogonal polarization, we use a Brewster window to reflect the probe and reference beams without significant reflection of the much stronger ionizing beam. While the probe and reference beams are well-separated when they are focused into the plasma, they overlap in the far field and form an interference pattern. This pattern, similar to a Young's double-slit pattern, is recorded using a CCD camera (CCD2 in Fig. 2). When the plasma is present, the position of this pattern shifts on the CCD camera. The optical delay stage allows us to measure the phase shift in this pattern due to the plasma as a function of time after the plasma is formed.

Measuring the fringe shift

The plasma density is measured by determining the phase shift of a probe laser beam as it passes through the plasma. The index of refraction of the plasma shifts the phase of the probe laser beam relative to the reference beam. Because the plasma's index of refraction is linearly proportional to the plasma density, we can use the fringe-shift data to determine the plasma density.

The index of refraction, \tilde{n} , of a plasma comprised of free electrons is given by

$$\tilde{n} = \sqrt{1 - \frac{(\omega_p^e)^2}{\omega_L^2}}. \quad (12)$$

As the index of refraction changes, the fringes in the interference pattern shift because of changes in the relative phase of the probe and reference laser beams,

$$\Delta\phi = \frac{2\pi\ell}{\lambda}(\Delta\tilde{n}) \approx \frac{2\pi\ell}{\lambda}n, \quad (13)$$

where ℓ is the length of the plasma and λ is the central wavelength of the laser pulse. The indexes of refraction for He, Ne, and Ar at 800 nm and standard temperature and pressure are 1.000035, 1.000066, and 1.00028, respectively [36]. For comparison, the index of refraction of the plasma at a wavelength of 800 nm and a density of 10^{18} cm^{-3} is 0.989, so the index of refraction of the background jet gas can be ignored.

The fringe shift, measured in pixel number on CCD2, is converted to phase by equating the period of the interference pattern to a phase shift of 2π . Then Eq. 13 is used to determine the density of the plasma. By changing the delay of the two weak beams relative to the strong laser beam, we measure the plasma density as a function of time.

THE PLASMA DENSITY

To a close approximation, strong-field ionization produces a plasma with a step-function density profile. As long as the atomic density is not too high, the atoms are ionized when the laser intensity is above the threshold intensities listed in Table 2. For moderate laser intensities, this produces a uniform density plasma with cylindrical symmetry. However, when the laser intensity is high enough to multiply-ionize the plasma, the plasma density is somewhat more complicated.

The laser intensity is Gaussian, of the form

$$I(r, z) = I_{pk} \left(\frac{1}{1 + z^2/z_r^2} \right) \exp \left[-\frac{2r^2}{w_0(1 + z^2/z_r^2)} \right], \quad (14)$$

where I_{pk} is the peak intensity, $z_r = \pi w_0^2/\lambda$ is the Rayleigh range, and w_0 is the Gaussian beam waist. When I_{pk} is greater than the intensities listed in Tab. 2, Eq. 14 defines a three-dimensional surface inside of which the atoms are

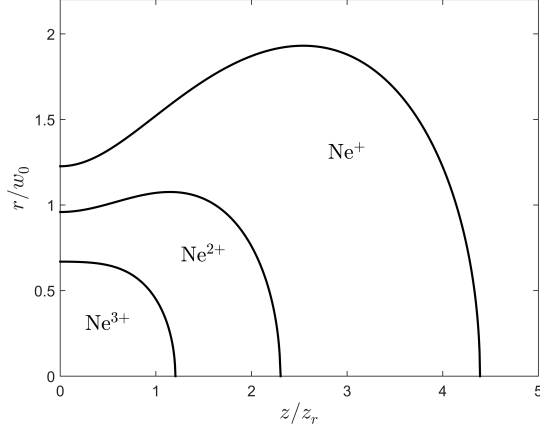


FIGURE 3. Ionization volumes in neon near the laser focus for $I_{pk} = (20) \times (8.7 \times 10^{14})$ W/cm². Using the r and z dependence of the intensity near Gaussian laser beam, given by Eq. 14, we can define volumes in which different ionization states are achieved. At low laser intensity, the plasma density is uniform. At high laser intensity, the initial plasma density has a “wedding cake” profile. In our experiment, the confocal parameter (twice the Rayleigh range) is longer than the plasma length, $z_r > \ell$, meaning that we can ignore the “blooming” of the ionization volume at larger z_r .

ionized. When the peak intensity is high enough to reach multiple ionization states, several surfaces are defined. In Fig. 3 we have plotted this for a high intensity pulse in neon, where the peak intensity is 20 times higher than the intensity required to reach the first ionization energy, $I_{pk} = 20 \times (8.7 \times 10^{14})$ W/cm².

For a single charge state, the plasma density is expected to evolve initially in a self-similar two-dimensional manner. This happens because the plasma density profile is cylindrically uniform with an abrupt cut-off in both radius (because of the intensity) and length (because of the gas jet geometry). With $\ell = 1$ mm and $w_0 \sim 10$ μ m, we can ignore expansion in the length and concentrate only on the radial expansion. As discussed in Ref. [33], the two-dimensional plasma evolution is expected to be of the form

$$n(t) = \frac{n(0)}{1 + \frac{v_e^2 t^2}{r_0^2}}, \quad (15)$$

where r_0 is the initial plasma size.

For a multi-step-function density distribution (see Fig. 3), some approximations need to be made to both the plasma size and the electron velocity. The plasma expansion depends on the initial size of the plasma, r_0 in Eq. 15. As most of the ions are in the volume dictated by the lowest ionization energy, we approximate the plasma size r_0 as the cut-off radius for the first ionization state. This cut-off radius depends on laser intensity as

$$r_n = w_0 \left[\frac{1}{2} \ln \left(\frac{I_{pk}}{I_n} \right) \right]^{1/2}, \quad (16)$$

where the subscript n labels the ionization state.

The expansion also depends on the expansion velocity, v_e . As discussed previously, the electron temperature is proportional to the ponderomotive energy at the field that ionizes that atom. The ponderomotive energy is linearly dependent on the intensity, and the intensity required to ionize the atom depends on the ionization energy as Φ^4 . Using Eqs. 6, 11, and the definition of the ponderomotive energy, we estimate the electron velocity as a volume-weighted average,

$$v_e^2 = 0.1 \left(\frac{\pi^2 \epsilon_0^2}{4m_e m_i \omega^2} \right) \frac{\sum \phi_n^4 r_n^2 / Z_n^2}{\sum r_n^2}, \quad (17)$$

where the n subscript refers to the ionization states (up to 3 in our experiments). Our laser interferometry method is sensitive only to the electron density. Because the electrons are light and the electron plasma frequency is high (see Tab. 1), the electrons are expected to thermalize quickly.

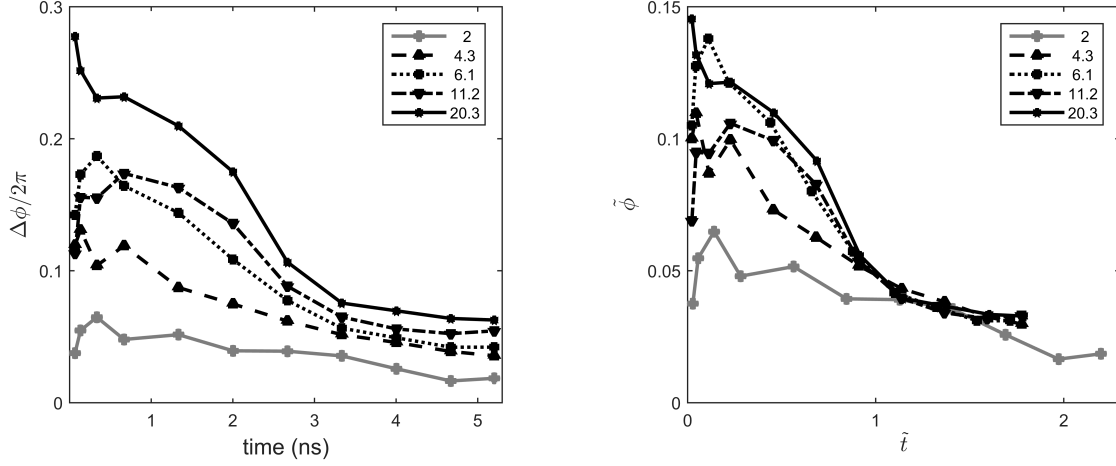


FIGURE 4. Left panel: A plot of the probe laser beam phase shift measurements in neon as a function of time after plasma formation. The peak laser intensities in these measurements range from 2 to 20.3 times the intensity required to reach the first ionization state in neon. Higher intensities show larger fringe shifts primarily due to the admixture of higher ionization states. Right panel: The scaled fringe shift plotted as a function of the scaled time. Except for the lowest laser intensity, proper scaling of the data shows the same time evolution.

The initial plasma density depends on the laser intensity. The average density in a plasma can be calculated using the expression

$$\tilde{n} = \frac{\sum_n r_n^2}{r_1^2}. \quad (18)$$

When a higher ionization state is reached, it adds one more electron per atom to the plasma.

MASS, ENERGY, AND RADIUS SCALING OF THE PLASMA EXPANSION

With this background, we can explore the mass, energy, and radius scaling of the plasma expansion. The mass scaling is straightforward, accomplished by using different gases in the jet. The energy scaling is accomplished by varying the laser intensity. This allows us to reach higher ionization states, corresponding to higher electron energies and faster plasma expansion. The radius scaling is folded into the energy scaling because the cut-off radius grows with laser intensity (see Eq. 16).

Energy and radius scaling

In Fig. 4 we plot measured phase-shift data as a function of time after plasma formation for a range of peak laser intensities. The laser intensities range from 2 to 20.3 times the minimum intensity required to reach Ne^+ . In general, higher intensities show a larger plasma phase shift. This happens primarily because of the admixture of higher ionization states in the plasma, increasing the electron density. Each point on the graph is an average of 200 laser shots at a particular intensity and given laser delay. In repeated measurements under identical conditions, we see that the measured fringe shift is strongly alignment dependent. We minimize this by focusing the probe laser beam to a smaller spot size than the ionizing laser beam. Still, shot-to-shot variations in laser power and pointing stability lead to some scatter in the data.

We can scale the phase shift data in the left-hand panel of Fig. 4 with density, velocity, and initial plasma size. Each of these depends on the laser intensity, as described previously. We first define a scaled phase shift,

$$\tilde{\phi} = \frac{\Delta\phi}{2\pi} \frac{1}{\tilde{n}}. \quad (19)$$

This scaled phase shift divides out the relative density of the plasma as higher ionization states are added.

We can also scale the time t using the electron velocity and initial plasma size. We define a scaled time variable,

$$\tilde{t} = \frac{v_e}{r_1}, \quad (20)$$

where the expansion velocity and r_1 are defined for the particular peak laser intensity used in the measurements.

Scaled this way, the expansion formula of Eq. 15 takes this form,

$$\tilde{\phi}(t) = \frac{\tilde{\phi}(0)}{1 + \tilde{t}^2} \quad (21)$$

The scaled data is plotted in the right panel of Fig. 4. Except for the lowest intensity data, this scaling puts all of the expansion data onto a similar curve. The lowest-intensity data is probably the most sensitive to any impurities in the plasma gas. Typical impurities, such as oxygen or nitrogen, will ionize at lower intensities, seeding electrons and ions into the plasma. These impurities become important at lower intensities primarily because we use the onset of plasma formation to estimate our peak laser intensity. Plasma formation at lower intensities (due to the lower ionization energies of these species) make impurities the dominant plasma constituent at low intensities. At higher intensities, the much higher density of the noble gas dominates plasma formation and evolution. It is interesting that both the electron expansion velocity and plasma size grow as the laser intensity increases. However the ratio is nearly constant.

Mass scaling

In principle, changing the ion mass in these plasmas is straightforward. However there are some technical difficulties that complicate the measurements somewhat. Certainly, changing the noble gas in the jet from He to Ne or Ar is trivial. However, these gases have different minimum ionization intensities. We reduce the peak intensity of the laser so that the value of I_{pk}/I_1 is the same for each gas. This is important if the radius of the gas is not changed. To avoid producing higher ionization states, the experiments must be performed with $I_{pk}/I_1 \approx 2$.

Measurements of the phase shift is shown for plasma measurements in He, Ne, and Ar in Fig. 5. For each gas, a neutral density filter was used to reach the same approximate value of $I_{pk}/I_1 \approx 2$, with I_1 given for each of the gases in Table 2. The symbols in Fig. 5 represent the measured phase shifts due to the plasma. The dashed lines are the corresponding fits using the model in Eq. 15. This model can be rewritten slightly as

$$n(t) = \frac{n(0)}{1 + t^2/\tau^2}, \quad (22)$$

where $\tau = v_e/r_0 = (0.1U_p/m_i)^{1/2}/r_0 \sim (I_n/m_i)^{1/2}/r_n$. This suggests that the relative values of τ for He, Ne, and Ar should be 1.0, 2.7, and 7.2. We use these values to generate the dashed lines shown in Fig. 5. The comparison between the data and the model shows the proper trend with mass. The maximum time in Fig. 5 is determined by the length of our delay line. Perhaps future work could explore delays at longer times.

A comparison of the characteristic expansion times from Fig. 5 using the previously mentioned relative values of τ , we find expansion times of 1.5, 4.1 and 11 ns for these gases. Taking the cut-off radius to be $0.59w_0$ with $w_0 = 20 \mu\text{m}$ (corresponding to $I_{pk}/I_1 = 2$), we find expansion velocities and electron energies for each of these three plasmas. The mass and intensity scaling of the data appears to be consistent. The results are summarized in Tab. 3

It is somewhat surprising that these electron temperatures in Tab. 3 are as low as they are. Based on work in ultracold plasmas, the plasma expansion is a good indicator of the electron temperature [10], with

$$k_B T_e = m_i v_e^2. \quad (23)$$

Our ionization model suggests that the electron energy should be higher, closer to $0.1U_p$. One possible explanation is that with our longer laser pulse (70 fs), ionization is occurring in the above-threshold-ionization (ATI) regime [35]. This would ionize our atoms at lower values of the field, meaning that we should use a smaller value of the ponderomotive energy. Another possibility is that our value for the initial plasma size is too small. Our ionizing laser is focused more tightly than in our previous work [33]. Energetic electrons may expand beyond the initial ionization volume ($\sim 14 \mu\text{m}$) and ionize neutral atoms in the surrounding gas. However, the electron-impact ionization cross-sections are too small for this to occur on the time scale of our experiment [37]. Ionization by ATI would increase the size of the initial plasma. Our strong-field model for ionization suggests that sharp plasma edge may be found at the radius given by Eq. 16. Sub-threshold ionization, such as ATI, would produce a larger radius. This issue could be explored in future work.

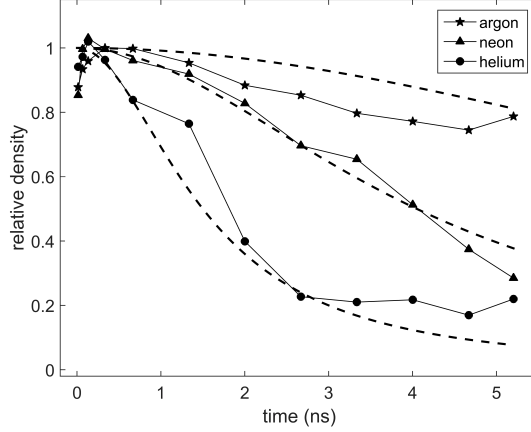


FIGURE 5. Measurement of the relative density of three plasmas in Ar, Ne, and He. These plasmas were measured at the same value of $I_{pk}/I_1 \approx 2$ to make sure the initial size of the plasma was constant. The same backing pressure was used in the jet for all three noble gases. The points represent the data. The lines are a fit using Eq. 15 as discussed in the text.

TABLE 3. Analysis of the expansion data from plasmas with different masses. The value of r_0 is based on our intensity data and consistent with measurements on CCD1. The expansion times τ are taken from the fits to the data in Fig. 5.

Atom	mass (amu)	r_0 (μm)	τ (ns)	v_e (m/s)	$m_i v_e^2$ (eV)	U_p	$m_i v_e^2 / U_p$
He	4	14	1.5	9300	3.6	155	0.023
Ne	20	14	4.1	3400	2.4	104	0.023
Ar	40	14	11	1300	0.7	30	0.023

MD SIMULATIONS

Before we end this paper, we would like to include some recent computational results related to achieving higher values of the Coulomb strong coupling parameter, Γ . Recently, we have studied sequential ionization in ultracold neutral plasmas [38]. In addition to this laser-jet experiment described so far, we also run experiments on resonantly photoionized laser-cooled calcium atoms [31]. A few years ago, one of us published a simulation that showed how sequential ionization of the plasma could increase the strong-coupling parameter without increasing the ion temperature [39, 40]. In that simulation, ions in an ultracold neutral plasma were promoted to the second ionization state at a particular time in the plasma evolution. This has been studied in more detail, both experimentally and computationally, in a recent publication by our group [38]. We will summarize some of the main ideas here. In particular, because it is relatively simple to reach the three-times-ionized states of Ne and even higher ionization states in Ar, Kr, and Xe, we would like to ask the question of how much one might increase the value of Γ if higher ionization states are reached.

To understand why sequential ionization boosts Γ without significantly raising the ion temperature, we need to look at the DIH process in a little more detail. As mentioned earlier in this document, atoms in a neutral gas have no spatial correlation. When these atoms are ionized, a repulsive interaction is suddenly turned on. Although the laser-cooled atoms have essentially zero kinetic energy, their electrical potential energy is very high. When this potential energy is converted to kinetic energy, the ion temperature increases. This is the disorder-induced heating process. In plasmas generated by photoionizing laser-cooled gases, the pre-DIH ion temperature is typically 0.01 K or less. After the DIH process, the ion temperature is several K, depending on the density (see Tab. 2).

The initial ion motion is partially coherent, in the sense that all the ions begin moving at the same time. The DIH kinetics are driven by nearest-neighbor interactions. In a plasma with uniform spatial density, the ions will collide with their neighbors at approximately the same time. The quasi-coherence of this motion results in a modest kinetic energy oscillation [28] because the ions start from rest, roll through a local minimum in their local potential well, and then slow down during a collision with their neighbors, all at roughly the same time.

When the ions pass through the minimum in their local potential landscape, the average nearest-neighbor potential

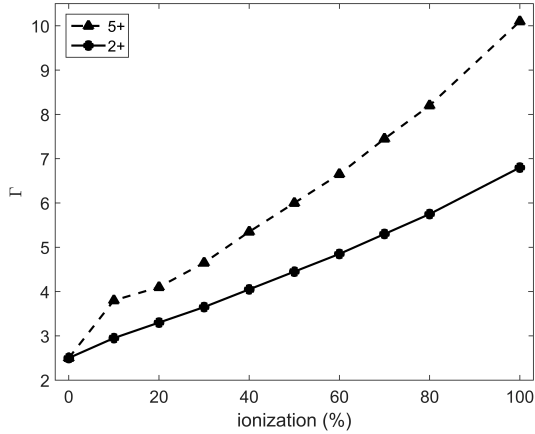


FIGURE 6. A calculation of the strong coupling parameter Γ as a function of the ionization fraction. In this calculation, plasma ions are promoted from the 1+ state to either the 2+ or the 5+ state. The timing of this second ionization event is timed to take advantage of the quasi-coherence in the ion motion during the DIH process. Details can be found in Ref. [38].

energy is at a minimum. At this moment, the ions could be promoted to the next higher ionization state. It would increase the potential energy while only minimally influencing the ion temperature. The details of our calculation and experiment are given in our recent publication [38].

We have studied the maximum value of Γ that can be achieved in this system as a function of the fraction of plasma ions that are promoted to the next ionization state. We found that when our laser-cooled Ca^+ ions are promoted to the Ca^{2+} state, the Coulomb coupling parameter increases from 2.5 to 6.8.

In light of the relative ease of reaching even higher ionization states in the fs-laser/plasma experiment we have described in this paper, we wondered what Γ values might be expected if instead of stopping at 2+, we went instead to 5+. The results are compared in Fig. 6.

For an optimized second ionization event, Γ increases from the nominal value of 2.5 that one normally expects from the DIH process to 6.8 if the final state is the doubly-ionized ion. If instead of going to 2+ the ions are promoted to 5+, the value of Γ increases only slightly to about 10. It may be possible to envision an optimized of ionization steps, passing through each ionization state in sequence. However, this seems technically challenging.

DISCUSSION

In this paper we have presented recent work in our group on laser-produced plasmas. Some characteristics of our plasmas are similar to ultracold neutral plasmas:

1. the ionization time and the electron plasma period are comparable,
2. the ion temperature is determined by the plasma density through the DIH process,
3. the hierarchy of time scales for electron and ion thermalization and plasma expansion are similar,
4. the initial ion density distribution suggests that the plasma expands in a self-similar fashion.

An important measurement that remains as yet unfinished in the fs-laser plasmas is a direct measurement of the ion temperature in the plasma. It could be measured relatively easily, at least in principle, because the noble gases have optical transition from the metastable states that can be excited using diode lasers. Because the number of atoms and the density are so high, the recombination rate may be large enough that laser-induced fluorescence measurements on recombined atoms are likely to be successful. Because recombination is a density- and temperature-dependent process, and because these quantities change in time, careful measurements are likely to be rich in plasma and atomic physics.

In the future, one could imagine focusing two or more high-intensity laser pulses into a gas jet and measuring the plasma density as these two strongly-coupled plasmas collide. This would be analogous to z-pinch plasma measurements, where arrays of exploding wires are used to create what is hoped to be a uniform plasma density

inside the array. In addition, new measurement techniques could be used to determine the plasma density. These might include the “Gabor” holography or one of the many other interferometric measurement methods used for high energy density plasma diagnostics.

ACKNOWLEDGMENTS

This research is supported by the National Science Foundation (Grant No. Phy-0969856) and the Air Force Office of Scientific Research (Grant No. FA9950-12-0308).

REFERENCES

1. D. H. Rischke, *Progress in Particle and Nuclear Physics* **52**, 197 (2004), ISSN 0146-6410.
2. H. M. VAN HORN, *Science* **252**, 384 (1991).
3. T. Bourdel, L. Khaykovich, J. Cubizolles, J. Zhang, F. Chevy, M. Teichmann, L. Tarruell, S. J. J. M. F. Kokkelmans, and C. Salomon, *Phys. Rev. Lett.* **93**, 050401 (2004).
4. I. B. Spielman, W. D. Phillips, and J. V. Porto, *Physical Review Letters* **98**, 080404 (2007).
5. V. Fortov, R. Ilkaev, V. Arinin, V. Burtzev, V. Golubev, I. Iosilevskiy, V. Khrustalev, A. Mikhailov, M. Mochalov, V. Ternovoi, and M. Zhernokletov, *Phys. Rev. Lett.* **99**, 185001 (2007).
6. B. Liu, and J. Goree, *Physical Review Letters* **100**, 055003 (2008).
7. J. M. Kriesel, J. J. Bollinger, T. B. Mitchell, L. B. King, and D. H. E. Dubin, *Phys. Rev. Lett.* **88**, 125003 (2002).
8. P. E. Grabowski, M. P. Surh, D. F. Richards, F. R. Graziani, and M. S. Murillo, *Phys. Rev. Lett.* **111**, 215002 (2013).
9. M. Lyon, S. D. Bergeson, and M. S. Murillo, *Phys. Rev. E* **87**, 033101 (2013).
10. S. Laha, P. Gupta, C. E. Simien, H. Gao, J. Castro, T. Pohl, and T. C. Killian, *Physical Review Letters* **99**, 155001 (2007).
11. G. Bannasch, T. C. Killian, and T. Pohl, *Phys. Rev. Lett.* **110**, 253003 (2013).
12. H. Sadeghi, A. Kruiyen, J. Hung, J. H. Gurian, J. P. Morrison, M. Schulz-Weiling, N. Saquet, C. J. Rennick, and E. R. Grant, *Phys. Rev. Lett.* **112**, 075001 (2014).
13. M. S. Murillo, *Phys. Rev. Lett.* **85**, 2514 (2000).
14. B. Liu, J. Goree, and Y. Feng, *Phys. Rev. Lett.* **105**, 085004 (2010).
15. T. Ott, D. A. Baiko, H. Kählert, and M. Bonitz, *Phys. Rev. E* **87**, 043102 (2013).
16. P. Hartmann, A. Douglass, J. C. Reyes, L. S. Matthews, T. W. Hyde, A. Kovács, and Z. Donkó, *Phys. Rev. Lett.* **105**, 115004 (2010).
17. L. Couëdel, S. Zhdanov, V. Nosenko, A. V. Ivlev, H. M. Thomas, and G. E. Morfill, *Phys. Rev. E* **89**, 053108 (2014).
18. T. Ott, and M. Bonitz, *Phys. Rev. Lett.* **103**, 195001 (2009).
19. M. J. Jensen, T. Hasegawa, J. J. Bollinger, and D. H. E. Dubin, *Phys. Rev. Lett.* **94**, 025001 (2005).
20. D. H. E. Dubin, *Phys. Rev. Lett.* **94**, 025002 (2005).
21. F. Anderegg, D. Dubin, T. O’Neil, and C. Driscoll, *Phys. Rev. Lett.* **102**, 185001 (2009).
22. E. E. Salpeter, *Austral. J. Phys.* **7**, 373 (1954).
23. E. E. Salpeter, and H. M. van Horn, *Ap. J.* **155**, 183 (1969).
24. S. Ichimaru, *Plasma Physics*, Benjamin/Cummings, Menlo Park, 1986.
25. M. E. Glinsky, T. M. O’Neil, M. N. Rosenbluth, K. Tsuruta, and S. Ichimaru, *Physics of Fluids B: Plasma Physics (1989-1993)* **4**, 1156 (1992).
26. M. S. Murillo, *Phys. Rev. Lett.* **87**, 115003 (2001).
27. M. S. Murillo, “Strongly coupled plasma physics and high energy-density matter,” AIP, 2004, vol. 11, pp. 2964.
28. Y. C. Chen, C. E. Simien, S. Laha, P. Gupta, Y. N. Martinez, P. G. Mickelson, S. B. Nagel, and T. C. Killian, *Phys. Rev. Lett.* **93**, 265003 (2004).
29. C. E. Simien, Y. C. Chen, P. Gupta, S. Laha, Y. N. Martinez, P. G. Mickelson, S. B. Nagel, and T. C. Killian, *Phys. Rev. Lett.* **92**, 143001 (2004).
30. T. C. Killian, S. Kulin, S. D. Bergeson, L. A. Orozco, C. Orzel, and S. L. Rolston, *Phys. Rev. Lett.* **83**, 4776 (1999).
31. E. A. Cummings, J. E. Daily, D. S. Durfee, and S. D. Bergeson, *Phys. Rev. Lett.* **95**, 235001 (2005).
32. J. P. Morrison, C. J. Rennick, J. S. Keller, and E. R. Grant, *Phys. Rev. Lett.* **101**, 205005 (2008).
33. N. Heilmann, J. B. Peatross, and S. D. Bergeson, *Phys. Rev. Lett.* **109**, 035002 (2012).
34. S. J. Augst, D. D. Meyerhofer, C. I. Moore, and J. Peatross, *Proc. SPIE* **1229**, 152 (1990).
35. G. G. Paulus, W. Nicklich, H. Xu, P. Lambropoulos, and H. Walther, *Phys. Rev. Lett.* **72**, 2851 (1994).
36. A. Bideau-Mehu, Y. Guern, R. Abjean, and A. Johannin-Gilles, *Journal of Quantitative Spectroscopy and Radiative Transfer* **25**, 395 (1981), ISSN 0022-4073.
37. R. Rejoub, B. G. Lindsay, and R. F. Stebbings, *Phys. Rev. A* **65**, 042713 (2002).
38. M. Lyon, S. D. Bergeson, A. Diaw, and M. S. Murillo, *Phys. Rev. E*, accepted for publication (2015).
39. M. S. Murillo, *Phys. Rev. Lett.* **96**, 165001 (2006).
40. M. S. Murillo, *Physics of Plasmas* **14**, 055702 (2007).